nature communications

Article

https://doi.org/10.1038/s41467-024-53948-1

Dynamic control and quantification of active sites on ceria for CO activation and hydrogenation

Received: 28 February 2024

Accepted: 29 October 2024

Published online: 07 November 2024

Check for updates

Weipeng Shao[1,5], Yi Zhang[2,5], Zhiwen Zhou[2,5], Na Li[2], Feng Jiao[2], Yunjian Ling[1,2], Yangsheng Li[1,2], Zeyu Zhou[1], Yunjun Cao[2], Zhi Liu[1], Xiulian Pan[2], Qiang Fu[2], Christof Wöll[3], Ping Liu[4], Xinhe Bao[2] & Fan Yang[1,2]

Ceria (CeO_2) is a widely used oxide catalyst, yet the nature of its active sites remains elusive. This study combines model and powder catalyst studies to elucidate the structure-activity relationships in ceria-catalyzed CO activation and hydrogenation. Well-defined ceria clusters are synthesized on planar CeO_2(111) and exhibit dynamic and tunable ranges of Ce coordination numbers, which enhance their interaction with CO. Reduced ceria clusters (e.g., Ce_3O_3) bind CO strongly and facilitate its dissociation, while near-stoichiometric clusters (e.g., Ce_3O_7) adsorb CO weakly and promote oxidation via carbonate formation. Unlike planar ceria surfaces, supported ceria clusters exhibit dynamic properties and enhanced catalytic activity, that mimic those of powder ceria catalysts. Insight from model studies provide a method to quantify active sites on powder ceria and guide further optimization of ceria catalysts for syngas conversion. This work marks a leap toward model-guided catalyst design and highlights the importance of site-specific catalysis.

Metal oxide catalysts are widely used in the chemical industry and have been increasingly explored for catalytic hydrogenation reactions[1–4], owing to their exceptional selectivity and stability. In syngas conversion, metal oxide nanocatalysts mixed with zeolites (OXZEO) exhibited exceptional catalytic performance[5], where metal oxides were proposed to play a key role in CO activation while oxide surfaces were conventionally believed to interact weakly with CO[6,7]. So far, our understanding of the active sites of metal oxide catalysts has been limited, which led to a rudimentary approach in evaluating their intrinsic catalytic properties, typically involving the normalization of the reaction rate against the total surface area of metal oxides.

To unravel the structure-activity relationship of metal oxide catalysts, planar oxide surfaces were frequently employed as model systems. Although they allow for atomic-scale insights into the surface structure of oxides[6,7] and can provide experimental information required for the validation of theoretical results[8], bridging the materials gap between model systems and synthesized powder catalysts remains a formidable task[9–12]. While the catalytic properties of oxides are often attributed to surface defects, model studies have predominantly focused on surface oxygen vacancy[1,13]. Coordinatively unsaturated (cus) metal sites[14–19] have also attracted increasing interest in past years and have been extensively studied on planar oxide catalysts such as RuO_2(110)[16,17,19], IrO_2(110)[15,19] and PdO(101)[18,19]. In contrast, practical metal oxide catalysts typically take the form of nanostructures (NSs)[20] and expose cus sites with diverse coordination numbers (CN)[21]. This complexity in their structure-activity relationship arises due to the interplay of several factors, including oxidation/electronic states, surface structural and compositional motifs, charge transfer, and unique size/shape characteristics[1,21–25]. To overcome

[1]School of Physical Science and Technology, Center for Transformative Science, ShanghaiTech University, Shanghai, China. [2]State Key Laboratory of Catalysis, Dalian Institute of Chemical Physics, Dalian, China. [3]Institute of Functional Interfaces, Karlsruhe Institute of Technology, Karlsruhe, Germany. [4]Chemistry Division, Brookhaven National Laboratory, Upton, New York, US. [5]These authors contributed equally: Weipeng Shao, Yi Zhang, Zhiwen Zhou. e-mail: fyang@shanghaitech.edu.cn

the intricate interdependencies in powder catalysts, it becomes imperative to study oxide NSs with tunable and well-defined surface structures, which enables the identification of active sites and the establishment of structure-activity relationships.

In this study, we synthesized well-defined oxide clusters on planar oxide surfaces, thereby facilitating an atomic-scale resolution of their intricacies. Using ceria catalysts as an example, our study integrated scanning tunneling microscopy (STM), synchrotron-radiation, and lab X-ray photoelectron spectroscopy (SRPES and XPS), density functional theory (DFT) calculations and model catalytic studies to examine their active-site structures and catalytic properties across a range of configurations by modifying the size, stoichiometry and CN of surface Ce sites (CN_{Ce})[26]. We demonstrated that supported ceria clusters mimicked the structural and redox dynamics of powder ceria[20,27–29], and controlled the reactivity of ceria in CO catalysis.

Ceria (CeO_x) is among the most widely used oxide catalysts in heterogeneous catalysis[30,31], and its superior catalytic performance is attributed to its ability to store and release oxygen[23], the formation of cus-Ce sites and the facile transition between different oxidation states[32]. Nonetheless, its active-site structure, adsorption, and catalytic properties have remained elusive. Through atomic-level studies of supported ceria clusters, planar ceria surfaces, and comparative analysis with powder ceria, we found that supported ceria clusters showed reaction properties similar to powder ceria and exhibited a dynamic and tunable range of CN_{Ce}, which correlates with CO activation and hydrogenation. The structure-reactivity relationship established through model studies can be extended to practical ceria catalysts and allow for the identification, quantification, and enhancement of active sites on ceria, leading to improved activity and selectivity for hydrocarbon production in syngas conversion.

Results and discussion

Synthesis of supported CeO_x model catalysts with different CN_{Ce}

Well-ordered CeO_2(111) thin films and supported CeO_x clusters were prepared (see "Methods" for details). Figure 1a, b shows that the CeO_2(111) surface displays flat terraces and exhibits an ordered hexagonal lattice with an atomic spacing of 0.38 nm and a step height of 0.3 nm, corresponding to the thickness of an O-Ce-O trilayer (Supplementary Fig. 1). Although surface and subsurface oxygen vacancies have been suggested as primary defects on CeO_2(111), their

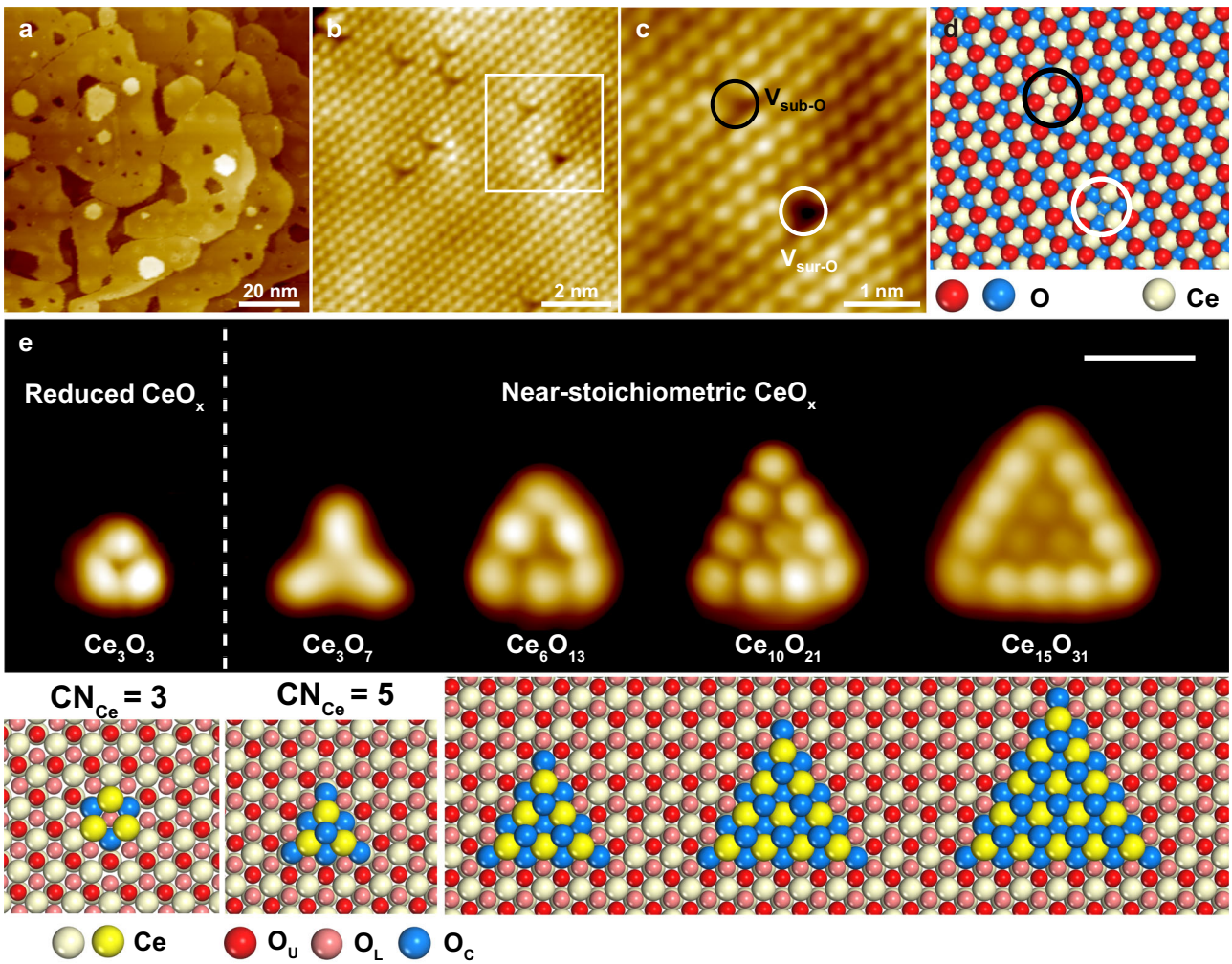

Fig. 1 | Atomic structures of planar CeO_2(111) and well-defined ceria clusters. **a** Large-scale STM image of the CeO_2(111) film surface. **b** O-mode STM image of the CeO_2(111) surface. The squared area is magnified in (**c**), showing surface O vacancy ($V_{sur\text{-}O}$) as a dark hole and sub-surface O vacancy ($V_{sub\text{-}O}$) as a three-pointed depression star at the hollow site of O atoms. The CeO_2(111) surface is dominated by $V_{sub\text{-}O}$. **d** The corresponding structural model of O vacancies. Ce atoms, surface, and subsurface O atoms are displayed in white, red, and blue, respectively. **e** Atomic-resolution STM images (upper panel, scale bar: 1 nm) and the corresponding structural models of supported Ce_3O_3, Ce_3O_7, Ce_6O_{13}, $Ce_{10}O_{21}$, and $Ce_{15}O_{31}$ clusters (lower panel). DFT-optimized structural models of Ce_3O_3 supported on Ce_2O_3(0001) and Ce_3O_7 supported on CeO_2(111) are displayed with labels on their O-coordination numbers of Ce sites. Surface lattice parameters are close for Ce_2O_3(0001) and CeO_2(111), which exhibited major differences in stacking along the vertical direction. O_U, O_L, and O_C represent O atoms in the topmost O layer, the lower O layer, and supported CeO_x clusters, respectively.

identification has remained elusive[25,33–35]. Using element-specific STM (ES-STM) imaging[36], we unambiguously identified surface and subsurface oxygen vacancies of CeO_2(111). The O-mode STM images resolved surface O atoms as bright protrusions, while surface O vacancies were depicted as dark holes (Fig. 1b–dand Supplementary Fig. 2a). Conversely, subsurface O vacancies manifested as three-pointed depressions at the hollow sites of surface O lattice (Fig. 1b, c). In the Ce-mode STM image (Supplementary Fig. 2b), Ce atoms were discerned as bright protrusions, and the structure of oxygen vacancies was not readily apparent (Supplementary Fig. 2c, d).

Ceria clusters of varying shapes and sizes were deposited on CeO_2(111) and exhibited high thermal stability at below 800 K[37]. CN_{Ce} of supported ceria clusters could be adjusted by regulating the O_2 pressure during Ce deposition (Fig. 1e). Here, we emphasize two types of surfaces that are stable under catalytically realistic conditions, which we termed as the near-stoichiometric CeO_x cluster (ns-CeO_x) and reduced CeO_x cluster (r-CeO_x) surfaces, respectively. The former surface could be prepared by evaporating Ce in above 3×10^{-7} mbar O_2, resulting in the formation of ns-CeO_x, such as Ce_3O_7, Ce_6O_{13}, $Ce_{10}O_{21}$, and $Ce_{15}O_{31}$ on CeO_2(111) with $CN_{Ce} \geq 5$ (Fig. 1eand Supplementary Fig. 3a). In contrast, the latter surfaces were prepared by evaporating Ce in 3×10^{-8} mbar O_2, leading to the growth of r-CeO_x, such as Ce_3O_3 or larger clusters on CeO_2(111) with lower CN_{Ce} (Fig. 1eand Supplementary Fig. 3c). As-prepared ceria clusters on both surfaces displayed a similar size distribution (Supplementary Fig. 3). Ce_3O_7 and Ce_3O_3 are the smallest clusters observed on each surface and could serve as the structural moiety for larger clusters, thus being representative of the oxidized and reduced states of ceria clusters on these two surfaces. Note that, the deposition of reduced CeO_x clusters could result in local reduction of the ceria substrate underneath, as indicated by the substantial reduction of CeO_2(111) in XPS (Supplementary Fig. 4). DFT calculations also showed that deposited Ce atom would reduce the neighboring substrate by pulling oxygen atoms towards Ce cations in reduced CeO_x clusters (Supplementary Fig. 4). Subsequently, Ce atoms underneath reduced CeO_x clusters tend to exhibit a structure similar to that of Ce_2O_3(0001)[38,39]. Highly reduced CeO_x clusters could be prepared by evaporating Ce atoms in UHV, but are not stable in CO at elevated temperatures (Supplementary Figs. 5, 6). Their reaction properties (Supplementary Figs. 5–7) are discussed in Supplementary Note 1 and are not the focus of this work.

Figure 1e demonstrates the diverse array of triangular supported CeO_x clusters, including Ce_3O_3, Ce_3O_7, Ce_6O_{13}, $Ce_{10}O_{21}$, and $Ce_{15}O_{31}$, which exhibited the same hexagonal lattice as CeO_2(111) but displayed varied sizes and CN_{Ce}. Their structures could be discerned from ES-STM images (Supplementary Fig. 8). From Ce_3O_3 to Ce_3O_7, both the Ce valence state (Supplementary Fig. 9) and CN_{Ce} increase, while the Ce lattice size remains mostly unchanged (Supplementary Fig. 3). As the cluster size expands from Ce_6O_{13}, $Ce_{10}O_{21}$ to $Ce_{15}O_{31}$, the alterations in valence state and CN_{Ce} are relatively insignificant, with clusters maintaining a near stoichiometry.

CO activation and hydrogenation over supported CeO_x model catalysts

Planar CeO_2(111) and supported CeO_x cluster surfaces were then exposed to CO respectively (Fig. 2) and showed drastically different reactivity towards CO. The CeO_2(111) surface that corresponded to a high CN_{Ce} of 7 showed no reactivity towards CO in UHV (Fig. 2a, b). Even after surface reduction to form $CeO_{1.93}$, no chemisorption or reaction of CO was obvious on planar ceria surfaces at 300 K from UHV to ambient pressures (AP) in STM or AP-XPS (Fig. 2a–cand Supplementary Fig. 10). CO appeared as diffusive species at step edges in STM at 78 K (Supplementary Fig. 11), but no CO reaction was obvious at between 300–500 K (Fig. 2d), as previously reported[40,41].

In contrast, supported ceria clusters demonstrated substantially higher reactivity towards CO. On the ns-CeO_x surface, Fig. 2e–h showed that adsorbates appeared at the corner or step sites of ceria clusters upon CO exposure at 300 K, and displayed similar apparent heights, often in the bidentate configuration. SRPES on the ns-CeO_x surface suggested the formation of $*CO_3$ species with a C *1 s* peak at 289.3 eV[42], which partially decreased at 500 K, and completely vanished at 600 K due to carbonate decomposition and CO_2 desorption (Supplementary Fig. 12). On the r-CeO_x surface, CO adsorption at 300 K produced a bright protrusion at the hollow site on Ce_3O_3 (Fig. 2i, j), displaying an apparent height of ~ 0.6 Å higher than carbonate on Ce_3O_7 (Fig. 2eand Supplementary Figs. 13, 14), and indicating a higher electronic density near the Fermi level (E_F). SRPES on the r-CeO_x surface detected an additional C *1 s* peak at 284.5 eV, suggesting the formation of *C (Fig. 2k, l), which could be produced via the disproportionation reaction of CO, simultaneously generating CO_2 and *C. CO_2 easily desorbed from the cluster surface, leaving *C at the hollow site. Among the different-sized ceria clusters, no noticeable size effect was observed on the formation of $*CO_3$ or *C species.

Spin-polarized DFT calculations were performed to understand the reaction properties of above supported CeO_x model catalysts. Based on STM measurements, Ce_3O_7 supported on CeO_2(111) (noted as Ce_3O_7) was constructed to represent the ns-CeO_x surface. Ce_3O_4 supported on Ce_2O_3(0001) (noted as Ce_3O_4), and Ce_3O_3/Ce_2O_3(0001) (noted as Ce_3O_3, Supplementary Fig. 15) were constructed to understand the r-CeO_x surface. In our study, the fully oxidized Ce_3O_7 cluster was stable only under the oxidizing conditions, and thus CeO_2(111) was used as support. As the reduced Ce_3O_4 and Ce_3O_3 clusters were synthesized under reducing conditions, the Ce_2O_3(0001) substrate was taken into consideration due to the possible removal of surface oxygen upon Ce deposition and the preferential diffusion of oxygen vacancies from surface to bulk of ceria[43]. DFT calculations showed that reduced CeO_x clusters supported on CeO_2(111) are not stable, but prefer to reduce the surface by pulling the oxygen atoms outward and form an atomic configuration (Supplementary Fig. 4a) similar to that of Ce_2O_3(0001) as reported previously[38]. The CeO_2(111) surface, Ce_2O_3(0001) surface and CeO_2(111) step were included for comparison. CO was used to probe the adsorption property of the most active Ce site (Supplementary Fig. 16) on each model system and found to prefer cus-Ce sites on all systems.

On planar ceria, both surface terraces and steps exhibited weak CO physisorption (Supplementary Fig. 16a, c) and no reaction with CO at 300 K (Fig. 2a–c). The binding energy of CO on Ce_3O_7 is also rather weak (− 0.21 eV) (Fig. 3aand Supplementary Fig. 16d), while the adsorption on Ce_3O_3 is strengthened by 0.79 eV (Fig. 3aand Supplementary Fig. 16f). Consistent with experimental studies, DFT results showed that indeed the weak Ce-CO interaction on Ce_3O_7 (Fig. 3b) results in the transition of adsorbed CO (*CO) to carbonate ($*CO_3$) species at the Ce_3O_7-CeO_2(111) interface, where a CO molecule interacts with oxygen from the corner site of Ce_3O_7 cluster, as well as O and Ce atom from the ceria support (Fig. 3c). In contrast, with the strong Ce-CO binding on Ce_3O_3/Ce_2O_3(0001) (Fig. 3a, d), the cleavage of the C-O bond to form atomic carbon (*C) is preferred (Fig. 3a, f), rather than the formation of $*CO_3$ (Fig. 3e). In this case, the breakage of C-O bond undergoes the CO disproportionation reaction ($2*CO \rightleftharpoons CO_2 + *C$, Fig. 3a, g), which is energetically more favorable than the direct dissociation of *CO ($*CO \rightleftharpoons *C + *O$, Fig. 3a, f). The Ce_3O_3/Ce_2O_3(0001) system allows the direct exposure of active Ce with low CN_{Ce} on the surface. As a result, the dissociated *C can be well stabilized at the three-fold hollow site of Ce atoms (Fig. 3g), as observed in STM (Fig. 2i). Thus, the reduction in CN_{Ce} from Ce_3O_7 to Ce_3O_3 along with the interfacial transformation could tune the favorable reaction pathway from the formation of $*CO_3$ to *C upon CO exposure, in agreement with experimental observations.

We then evaluated the influence of cluster size, the oxidation state of Ce and CN_{Ce} in CO activation using CO adsorption energy as an indicator. A correlation could be observed for CO adsorption at the Ce site in the range of $3 \leq CN_{Ce} \leq 7$ (Supplementary Fig. 17). The CO binding energy increases with the contraction of the Ce-C bond, and

https://doi.org/10.1038/s41467-024-53948-1

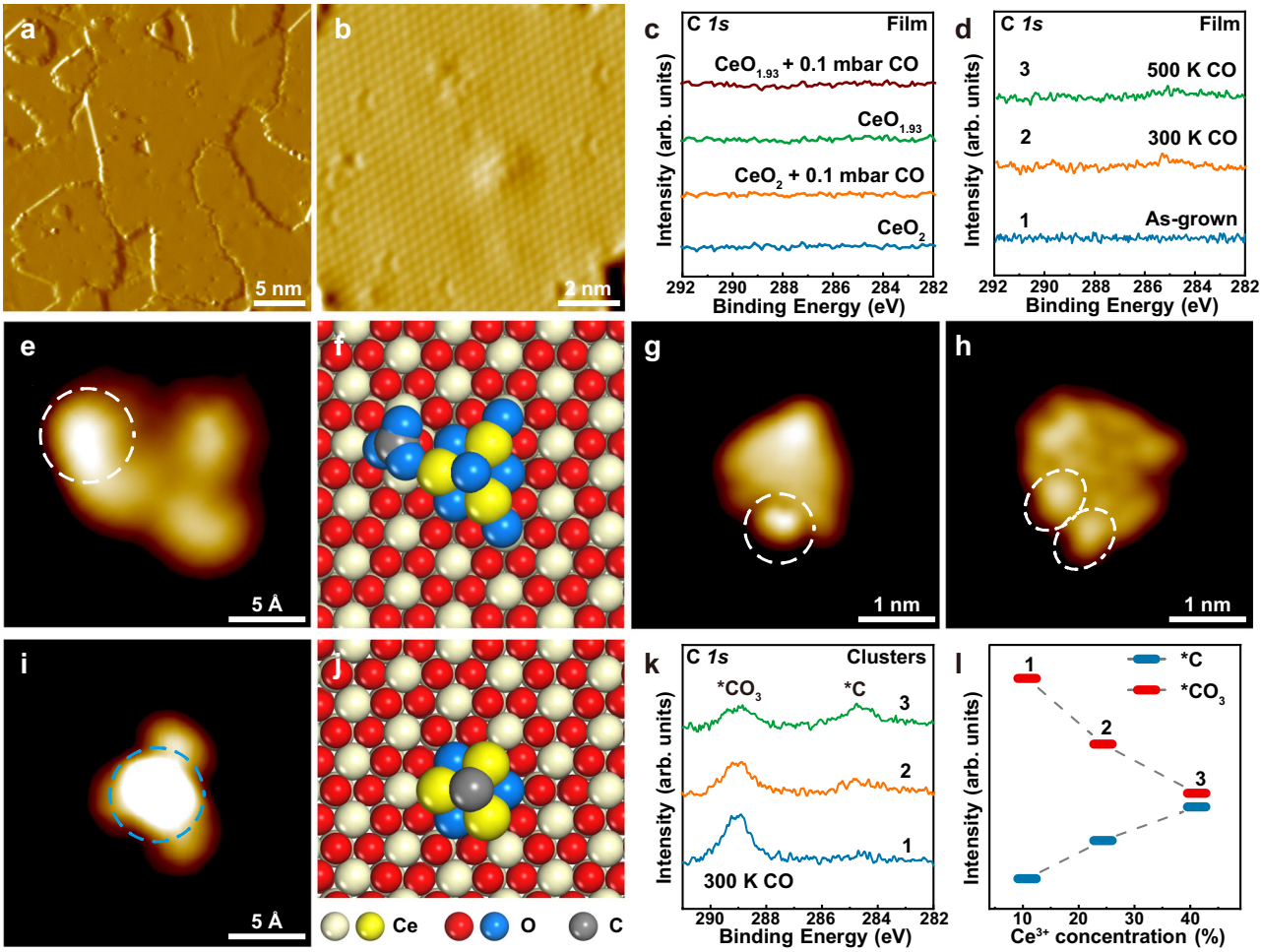

Fig. 2 | CO interaction and reaction with the CeO_2(111) surface and ceria clusters supported on CeO_2(111). **a**, **b** STM images of the CeO_2(111) surface after the exposure to 250 L CO at 300 K. **c** C *1 s* spectra of planar CeO_2(111) and reduced CeO_{2-x}(111) surfaces before and after the exposure to 0.1 mbar CO at 300 K. The stoichiometry of the reduced CeO_{2-x}(111) surface was determined as $CeO_{1.93}$ by XPS Ce *3 d* spectra. **d** C *1 s* spectra of the CeO_2(111) film taken after sequential treatments: 1. the as-gown film; 2. the exposure of 250 L CO at 300 K; 3. the annealing to 500 K in 5×10^{-7} mbar CO and then cooling to 300 K in CO. **e**–**h** STM images of (**e**) Ce_3O_7, (**g**) $Ce_{15}O_{31}$ and (**h**) $Ce_{21}O_{43}$ clusters after the exposure to 5×10^{-7} mbar CO at 300 K. The corresponding structural model of Ce_3O_7 after CO adsorption was shown in (**f**). Adsorbate could be observed at the corner site of Ce_3O_7 and along the step/corner sites of $Ce_{15}O_{31}$ and $Ce_{21}O_{43}$. **i** STM image of Ce_3O_3 after the exposure to 5×10^{-7} mbar CO at 300 K. Adsorbate could be observed at the hollow site, and the corresponding structural model was shown in (**j**). **k** C *1 s* spectra of supported ceria clusters taken after exposing to 250 L CO at 300 K (1. the ns-CeO_x surface; 2. supported ceria clusters prepared by evaporating Ce in 1×10^{-7} mbar O_2 at 300 K onto CeO_2(111); 3. the r-CeO_x surface). The intensities of carbonate and carbon peaks from (**k**) are plotted in (**l**), as a function of surface Ce^{3+} concentration, which was obtained from RPES taken simultaneously.

the decreasing of CN_{Ce} for the Ce site interacted (Supplementary Figs. 16, 17). Neither the oxidation state of Ce nor cluster size appeared as sensitive as CN_{Ce}. A decrease in the oxidation state of Ce from 4 + to 3 + could only increase CO binding by 0.07 eV when CN_{Ce} was kept at 6 for the CeO_2(111) step and Ce_2O_3(0001) surface. Meanwhile, for Ce_3O_x of similar cluster size, a significant increase in CO binding could be observed from Ce_3O_7 (− 0.21 eV) to Ce_3O_4 (− 0.82 eV) and Ce_3O_3 (− 1.0 eV). The mixed influence of CN_{Ce} and electronic effect cannot be disentangled for Ce_3O_x. However, DFT calculations corroborated that the enhanced reactivity of supported ceria clusters could be associated with a significant gain in the flexibility of Ce_3O_x (Supplementary Table 1 and Supplementary Note 2). Such flexibility enables variations in the local environment[21] around the interacted Ce site to accommodate and enhance the interaction with CO.

Structural dynamics and catalytic properties of supported CeO_x model catalysts during CO hydrogenation

The flexibility of supported Ce_3O_x clusters could be further demonstrated by their enhanced reactivity and structural dynamics in CO hydrogenation (Fig. 4). When planar CeO_2(111) was exposed to the flowing CO/H_2 (1:3) mixture gas, no appreciable reactivity was detected by on-line GC from 300 to 675 K (Supplementary Fig. 18). In contrast, when the ns-CeO_x surface was heated in the same CO/H_2 mixture gas, two main products, CO_2 and CH_4, were observed throughout the reaction, with the former easily detected at above 500 K and the latter at above 575 K (Supplementary Fig. 18). Despite the similar oxidation state of planar ceria and the ns-CeO_x surface (Fig. 4c), they exhibited orders-of-magnitude reactivity difference for CO hydrogenation. Quasi-in-situ XPS analysis suggested a significant reduction of Ce sites on the ns-CeO_x surface from 5.6% to 42.3% (Fig. 4c, d), whereas planar ceria surfaces were only reduced from 3.2% to 8.9%.

On the ns-CeO_x surface, two kinetic regimes were observed for the formation of CO_2 (Fig. 4a), with the low-temperature regime requiring a high barrier (125 kJ/mol) and the high-temperature regime displaying a low barrier of 22.0 kJ/mol. The formation of CH_4 in the high-temperature regime exhibited an apparent activation energy of 72.0 kJ/mol (Supplementary Fig. 18c). Interestingly, the r-CeO_x surface showed an oxidation state similar to that of the ns-CeO_x surface after

https://doi.org/10.1038/s41467-024-53948-1

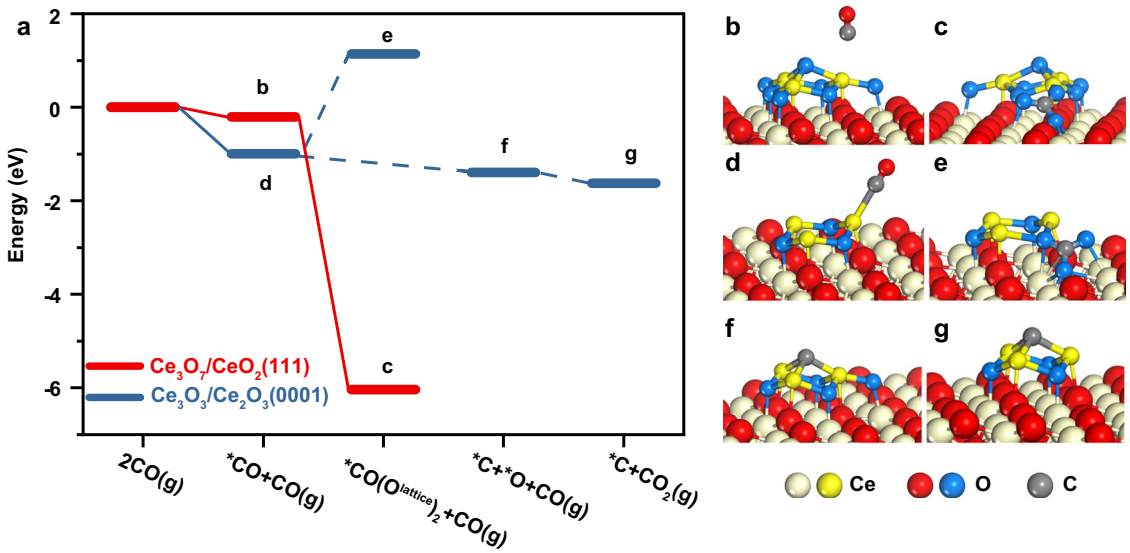

Fig. 3 | DFT-calculated potential energy diagram for the reaction toward CO on $Ce_3O_7/CeO_2(111)$ and $Ce_3O_3/Ce_2O_3(0001)$. a Reaction diagram together with the optimized geometries of reaction intermediates: (**b**) *CO and (**c**) $*CO_3$ on $Ce_3O_7/CeO_2(111)$, (**d**) *CO, (**e**) $*CO_3$, (**f**) *C + *O and (**g**) *C on $Ce_3O_3/Ce_2O_3(0001)$.

CO hydrogenation (Fig. 4c, d). When the as-prepared r-CeO_x surface was exposed to the same CO/H_2 mixture gas, an onset production of CO_2 yielded an apparent activation energy of 22.1 kJ/mol (Fig. 4b) and the production of CH_4 yielded an apparent activation energy of 71.8 kJ/mol (Supplementary Fig. 19), similar to those of the ns-CeO_x surface in the high-temperature regime. Post-reaction analysis of the r-CeO_x surface also showed a similar Ce oxidation state and C *1 s* spectra as those of the ns-CeO_x surface after CO hydrogenation (Fig. 4d, e). XPS C *1 s* spectra suggested that both surfaces resulted in a facile CO disproportionation reaction to produce CO_2 and *C (Fig. 4e), as also demonstrated by the r-CeO_x surface in UHV (Fig. 2i, k). In the CO/H_2 mixture gas, the *C species were subsequently hydrogenated to produce CH_4. Combining reaction kinetics and XPS analysis suggested that a high-pressure CO hydrogenation reaction could reduce the ns-CeO_x surface into the r-CeO_x surface, which involved an induction period and resulted in the low-temperature kinetic regime of ns-CeO_x, where the decomposition of carbonate to CO_2 requires a large barrier[44]. Only upon the reduction to the r-CeO_x surface did the disproportionation reaction of CO become feasible, producing CO_2.

While the *C and $*CO_3$ species were observed on the ns-CeO_x and r-CeO_x surfaces after CO hydrogenation, planar ceria surfaces remained clean throughout the reaction range up to 675 K (Fig. 4e). The limited reactivity of planar ceria surfaces could originate from the lack of surface cus-Ce sites ($CN_{Ce} \leq 5$). ES-STM images have suggested that oxygen vacancies are concealed in $CeO_2(111)$ and preferentially located at subsurfaces (Fig. 1b), while the surface consists of < 1% O vacancies. Even after the reduction by CO at 800 K and above, we did not observe an obvious change in the density of surface O vacancies (Supplementary Fig. 20). The reduction in Ce oxidation state, in this case, is not indicative of active sites on planar ceria.

In contrast to planar $CeO_2(111)$, the drastic reduction of ns-CeO_x to r-CeO_x and its superior activity imply a significant role of cus-Ce sites on ceria clusters in CO hydrogenation under catalytically realistic conditions. By varying CN_{Ce}, not only the binding properties of Ce sites can be tuned, thus enhancing their catalytic activity, but also new reaction routes can be opened, thus changing selectivity. Our study shows that planar CeO_2 surfaces tend to conceal oxygen vacancies inside the bulk, and eventually transform to Ce_2O_3 at the surface layer, making it challenging to form cus-Ce sites active towards CO. In contrast, such cus-Ce sites are predominantly exposed at the edges of supported ceria clusters, which enable enhanced activity and tuned selectivity.

Quantification of active sites and improving powder ceria catalysts for CO hydrogenation

The dynamic transformation between ns-CeO_x and r-CeO_x surfaces, as well as their adsorption and catalytic properties, are indeed analogous to those of powder ceria catalysts during CO activation and hydrogenation (Fig. 4c, d). Powder ceria catalysts, typically in the shape of nanoparticle (CeO_2-N) or rod (CeO_2-R), were synthesized and all exhibited the same fluorite structure (Supplementary Fig. 21). A series of CeO_2-N catalysts were prepared by varying their calcination temperatures at 673 K, 1073 K, and 1473 K, which were named CeO_2-673, CeO_2-1073, and CeO_2-1473, respectively. From X-ray diffraction (XRD), these ceria catalysts exhibited different average crystallite sizes at 7.9, 75, and 117 nm (Supplementary Table 2and Fig. 21). Meanwhile, a CeO_2-R catalyst was prepared and calcined at 573 K, termed as CeO_2-573, with an average crystallite size of 9.9 nm (Supplementary Table 2). The morphology, crystal facets, and particle size of these synthesized powder catalysts (Supplementary Fig. 22) were confirmed by high-resolution transmission electron microscopy (TEM), corroborating with XRD analysis.

Upon CO exposure at room temperature, our FT-IR measurements (Supplementary Fig. 23a) showed the spontaneous formation of $*CO_3$ species, in agreement with FT-IR studies[10,45]. Upon the reduction by CO, the formation of surface *C species, in addition to $*CO_3$, could be further observed in XPS on ceria catalysts (Supplementary Fig. 23b). Meanwhile, an online mass spectrometer (MS) detected CO_2 production at above 473 K, and the subsequent annealing in H_2 resulted in the observation of hydrocarbons such as ionized CH_4 and C_2H_x species, indicating CO disproportionation reaction on ceria (Supplementary Fig. 24).

When powder ceria was employed for CO hydrogenation, an induction period for the production of CO_2 was observed (Supplementary Fig. 25a), similar to that on the ns-CeO_x surface. However, when powder ceria was pre-reduced in H_2, the induction period was eliminated, and a steady-state CO_2 production could be observed with a reaction rate similar to that without H_2 treatment (Supplementary Fig. 25b, c). Thus, the observed CO hydrogenation activities on powder ceria depend strongly on the low CN_{Ce} sites generated under reducing conditions, as demonstrated in model studies. Post-reaction XPS analysis showed a significant reduction of powder ceria during CO hydrogenation, which led to the concentration increase of Ce^{3+} sites from ~ 4% to 46.2% (Fig. 4c, d), similar to the behavior of the ns-CeO_x surface. The similar adsorption and reaction properties between powder ceria and the ns-CeO_x surface suggested that Ce_3O_7 could

https://doi.org/10.1038/s41467-024-53948-1

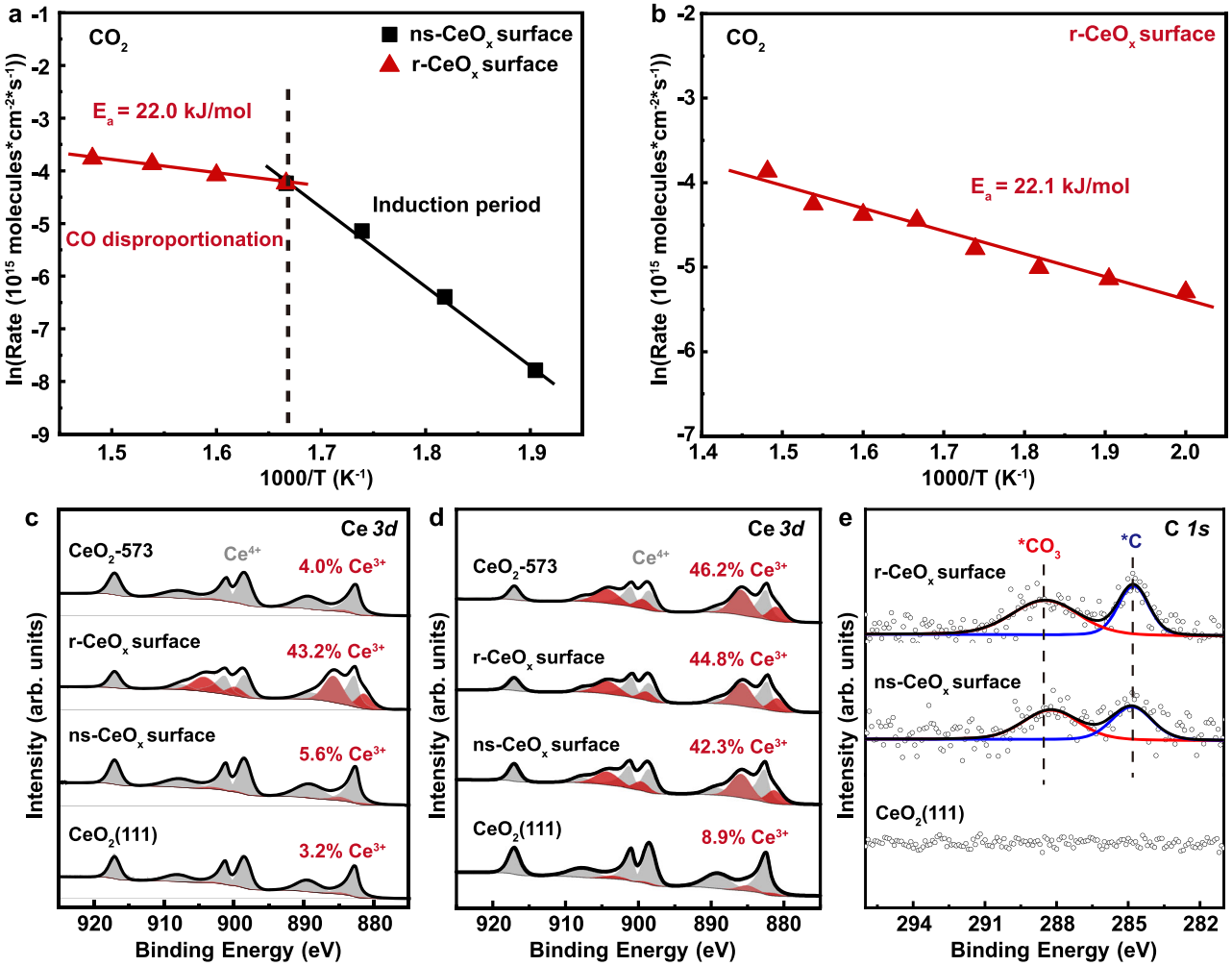

Fig. 4 | Comparison of reaction kinetics, surface valance states, and chemical properties of model and powder ceria catalysts. The Arrhenius plots of reaction rates for CO hydrogenation to CO_2 were displayed for (**a**) the ns-CeO_x surface and (**b**) the r-CeO_x surface. XPS Ce *3 d* spectra of planar CeO_2(111), the ns-CeO_x surface, the r-CeO_x surface, and CeO_2-573 catalysts were compared (**c**) before and (**d**) after the CO hydrogenation reaction. **e** XPS C *1 s* spectra of the ns-CeO_x surface, the r-CeO_x surface, and planar CeO_2(111) after the CO hydrogenation reaction.

serve as a structural analog for active sites on powder ceria, which underwent the same reductive transformation as the transformation from ns-CeO_x to r-CeO_x surfaces under CO hydrogenation reaction condition. As such, model understanding acquired from ns-CeO_x/r-CeO_x surfaces could guide the quantification and optimization of active sites on practical ceria catalysts.

Our model studies have shown that supported ceria clusters were not stable at above 800 K. Thus, varying the calcination temperature of powder ceria might be able to control the surface density of active sites. The series of ceria catalysts calcined at varying temperatures were tested for CO hydrogenation. Figure 5 showed that the space-time yields[46] of hydrocarbon increase from 38 μmol·g_{ox}^{-1}·h^{-1} for CeO_2− 1473 to 1336 μmol·g_{ox}^{-1}·h^{-1} for CeO_2− 573 with decreasing calcination temperature. The increase in space-time yield remains distinct from CeO_2− 673 (966.8 μmol·g_{ox}^{-1}·h^{-1}) to CeO_2-573 despite their similar crystallite size from XRD (Supplementary Table 2). XPS Ce *3 d* spectra (Supplementary Fig. 26) showed that four ceria catalysts all exhibited similar concentrations of Ce^{3+} sites (~ 4%) upon calcination. Thus, XPS measurement of Ce oxidation state or XRD measurement of ceria crystallite size is not sensitive to active sites on powder ceria catalysts[21].

However, the above model studies have shown that active sites on ceria are susceptible to carbonate formation upon CO exposure. That means, IR measurements of surface carbonates could be employed to quantify active sites on powder ceria and showed drastic intensity differences among the four ceria catalysts (Supplementary Fig. 27). Indeed, reaction rates of these ceria catalysts were found to scale linearly with the normalized carbonate intensity from IR (Fig. 5), regardless their different size, shape or oxidation state. Our results confirm that the calcination treatment could be used to control the density of active Ce sites on powder ceria for CO activation and CO hydrogenation, which could be probed by IR.

To promote the catalytic performance of CO hydrogenation, we further mixed CeO_2-T (T = 573, 673, 1073, 1473) catalysts with SAPO-34 zeolites. Previous study[5] suggested that adding zeolites could greatly facilitate the conversion of CH_x species produced on partially reduced oxides into hydrocarbons, thereby pushing the reaction equilibrium of CO conversion forward. Consistently, the addition of SAPO-34 significantly increased CO conversion and selectivity towards light olefins (Fig. 5band Supplementary Fig. 28). In combination with SAPO-34, CeO_2-573 achieves a much higher CO conversion of 19.7% than other CeO_2-T catalysts. The activity of mixed catalysts (CO conversion) still exhibited a linear relationship with the active-site density measured from normalized carbonate intensity, rather than with the particle size or oxidation state of powder ceria.

In summary, the combined model and powder catalytic studies demonstrated the pivotal role of dynamically transforming ceria

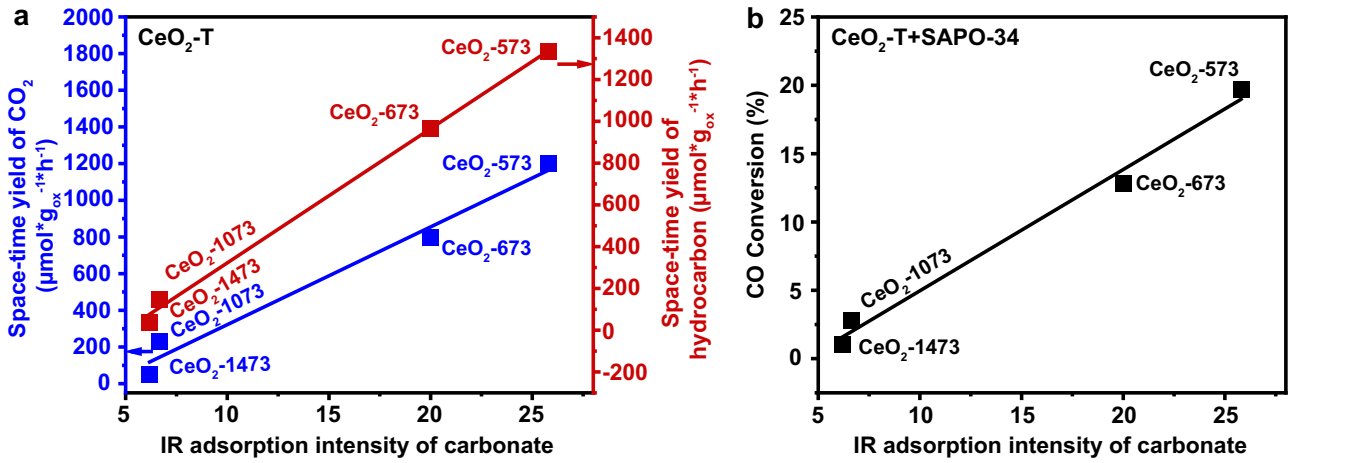

Fig. 5 | The relationship between syngas conversion performance and the surface density of active sites on (a) CeO_2-T and (b) CeO_2-T/SAPO-34 (T = 573, 673, 1073, 1473 K). The surface densities of active sites were measured by IR adsorption intensity of surface carbonate normalized by IR adsorption intensity of CO at 130 K. Reaction conditions for syngas conversion: CO/H_2 = 1/2.5, 673 K, 4.0 MPa and gas hourly space velocity (GHSV) = 2400 mL·h^{-1}·g_{ox}^{-1}, CeO_2/SAPO-34 = 2/1 (mass ratio) in composite. The absorbance of carbonate was derived from FT-IR spectra after exposing CeO_2-T catalysts to CO at 300 K.

clusters in CO activation and hydrogenation. By synthesizing well-defined ceria clusters on planar CeO_2(111) with tailored CN_{Ce}, we examined their structures, adsorption, and catalytic properties at the atomic level with an integrated approach using STM, SRPES, XPS, DFT calculations, and model catalytic studies. In contrast to planar ceria surfaces, supported ceria clusters exhibited dynamic and tunable ranges of CN_{Ce}, which correlates with their much-enhanced activity towards CO activation and hydrogenation. We found that r-CeO_x (e.g., Ce_3O_3) binds CO strongly and facilitates CO dissociation to atomic carbon and subsequent hydrogenation, whereas ns-CeO_x (e.g., Ce_3O_7) binds CO weakly and preferentially promotes CO oxidation via carbonate formation.

Importantly, the dynamic reduction of the ns-CeO_x surface to the r-CeO_x surface during CO hydrogenation demonstrates the flexibility of supported ceria clusters similar to powder ceria catalysts. Atomic-level understanding from model studies could transfer effectively to practical ceria catalysts. We showed that their catalytic activity for CO hydrogenation can be distinguished by neither the particle size from XRD nor the Ce oxidation state from XPS. Rather, active sites on ceria could be titrated via carbonation formation as suggested by model studies and measured from IR. The carbonate intensity showed a linear relationship with CO conversion over ceria or its composite catalysts. By modulating the pre-treatment and activation procedures to maximize active site density, we improved the performance of powder ceria catalysts for CO hydrogenation. The understanding of active sites on ceria and the methodologies developed in this study could have general implications for studying complex oxide catalysts.

Methods

Model catalyst preparation and characterization

STM experiments were carried out in a combined ultrahigh vacuum (UHV) system, equipped with low-temperature scanning tunneling microscopy (LT-STM, Createc), XPS, UPS, and the cleaning facilities. The base pressures of STM and the preparation chamber are 4×10^{-11} and 5×10^{-11} mbar, respectively. All STM images were taken at 78 K and processed with SPIP software from Image Metrology (Denmark). Synchrotron-radiation photoelectron spectroscopy (SRPES) measurements were performed at the BL11U beamline in the National Synchrotron Radiation Laboratory (NSRL), China. The end station of the BL11U beamline is a combined UHV system including the analysis chamber, the preparation chamber, molecular beam epitaxy (MBE) chamber, and a radial distribution chamber. The base pressures are 7×10^{-11}, 1×10^{-10}, 5×10^{-10}, and 2×10^{-11} mbar, respectively. The analysis chamber is equipped with a VG Scienta R4000 analyzer, a monochromatic Al K_α X-ray source, a UV light source, low energy electron diffraction (LEED), and a flood electron gun.

Well-ordered CeO_2(111) thin film was prepared on Pt(111) by evaporating Ce in 1×10^{-7} mbar O_2. Pt(111) single crystal (MaTeck) was cleaned by cycles of Ar ion sputtering and annealing up to 1000 K. Surface cleanness was verified by STM and XPS. To ensure the full coverage of the metal substrate and the crystalline quality of ceria thin film, a kinetically limited growth process was adopted to grow CeO_2(111)[22]. STM studies on as-prepared CeO_2(111) thin films with varying thickness observed the same surface structure and found no obvious change in the concentration of surface defects on CeO_2(111) (Supplementary Fig. 29). For reactivity measurements, CeO_2(111) single crystals (Surfnet, Germany) and CeO_2(111)/YSZ(111) were used to remove the influence of metal substrates. Supported ceria clusters of different CN_{Ce} were prepared on CeO_2(111) by controlling the O_2 pressure for Ce deposition. Details of model catalyst preparation and characterization are given in Supplementary Methods.

Powder catalyst preparation and characterization

CeO_2 powder catalysts were prepared by precipitating cerium nitrate with urea in aqueous solution[47]. 21.71 g $Ce(NO_3)_3$·$6H_2O$ (Aladdin, AR), 12.61 g $C_2H_2O_4$ (tansoole, AR), and 9.01 g $CO(NH_2)_2$ (General-reagent, AR) were added into 50 mL distilled water with continuous stirring for 1 h. Then the mixed solution was transferred into a 100 mL autoclave and heated to 413 K for 12 h. After filtering and washing several times with distilled water, the resulting precipitates were dried overnight at 353 K and then calcined at 673 K for 3 h. The obtained catalyst was named CeO_2-673. The catalysts CeO_2-1073 and CeO_2-1473 were prepared by further calcining CeO_2-673 at 1073 K and 1473 K in air for 3 h separately.

Powder ceria with an average crystal size of 9.9 nm was synthesized by a hydrothermal method. First, 24.0 g NaOH (General-reagent, AR) was added to $Ce(NO_3)_3$·$6H_2O$ (Aladdin, AR) (1.736 g to 80 mL of Millipore water) with continuous stirring for 0.5 h. Then the mixed solution was transferred into a 100 mL autoclave and heated to 383 K for 24 h. After filtering and washing several times with distilled water, the resulting precipitates were dried overnight at 333 K and then calcined at 573 K for 3 h. The obtained catalyst was named CeO_2-573.

X-ray diffraction (XRD), N_2 adsorption-desorption, X-ray photoelectron spectroscopy (XPS), Fourier Transform infrared spectroscopy

(FT-IR), Transmission electron microscopy (TEM) and temperature-programmed surface reaction (TPSR) were used to measure the size, surface area, valence state, CO interaction with powder ceria, morphology and reactivity of ceria catalysts. The catalytic activity was measured in a fixed-bed reactor. Details of powder catalyst characterization are given in Supplementary Methods.

Catalytic activity measurements

Reactivity measurements on model catalytic systems were performed on planar CeO_2(111) surfaces and supported ceria clusters during CO hydrogenation in a high-pressure quartz fixed bed reactor cell (HPRC). HPRC was directly connected to a UHV system, consisting of an XPS (Thermo-Fisher ESCALAB 250Xi) chamber and an MBE chamber. XPS was used to monitor catalyst samples before and after the reaction. Both CeO_2(111) single crystals and CeO_2(111)/YSZ(111) were tested and showed little differences from the substrates. Details of reactivity measurements and powder catalytic tests are given in Supplementary Methods.

Computational methods

DFT calculations were performed with the Perdew-Burke-Ernzerhof (PBE) exchange-correlation functional[48,49] in a projector augmented-wave (PAW) implementation[50] using the Vienna ab initio simulation packages (VASP). A cutoff energy of 400 eV for the plane-wave basis set was employed for slab calculation and 700 eV for bulk calculation to obtain optimized lattice parameters. To obtain faster convergence, thermal smearing of one-electron states ($k_BT = 0.05$ eV) was allowed using the Gaussian smearing method to define the partial occupancies. The DFT + U formalism was used to describe the localized (strongly correlated) *4f* electrons in cerium, as implemented by Dudarev[51]. To describe Ce, $U_{Ce} - J_{Ce} = 3.0$ eV was used, which was shown previously to describe the surface chemistry of ceria appropriately with the DFT(GGA) + U method[52–54]. All structures were well converged until the forces decreased to less than 0.02 eV/Å. More details on the model construction and computation are described in Supplementary Methods.

Data availability

The data that support the findings of this study are available from the corresponding authors upon request. Source data are provided in this paper.

References

1. Vohs, J. M. Site requirements for the adsorption and reaction of oxygenates on metal oxide surfaces. *Chem. Rev.* **113**, 4136–4163 (2013).
2. Stacchiola, D. J., Senanayake, S. D., Liu, P. & Rodriguez, J. A. Fundamental studies of well-defined surfaces of mixed-metal oxides: Special properties of MO_x/TiO_2(110) {M = V, Ru, Ce, or W}. *Chem. Rev.* **113**, 4373–4390 (2013).
3. Dai, Y. et al. Recent progress in heterogeneous metal and metal oxide catalysts for direct dehydrogenation of ethane and propane. *Chem. Soc. Rev.* **50**, 5590–5630 (2021).
4. Vilé, G., Bridier, B., Wichert, J. & Pérez-Ramírez, J. Ceria in hydrogenation catalysis: High selectivity in the Conversion of Alkynes to Olefins. *Angew. Chem. Int. Ed.* **51**, 8620–8623 (2012).
5. Jiao, F. et al. Selective conversion of syngas to light olefins. *Science* **351**, 1065–1068 (2016).
6. Diebold, U., Li, S. C. & Schmid, M. Oxide surface science. *Annu. Rev. Phys. Chem.* **61**, 129–148 (2010).
7. Henrich, V. E. & Cox, P. A. *The Surface Science of Metal Oxides*. (Cambridge University Press, England, 1996).
8. Lustemberg, P. G. et al. Vibrational frequencies of Cerium-Oxide-Bound CO: A challenge for conventional DFT methods. *Phys. Rev. Lett.* **125**, 256101 (2020).
9. Wang, Y. M. & Wöll, C. IR spectroscopic investigations of chemical and photochemical reactions on metal oxides: bridging the materials gap. *Chem. Soc. Rev.* **46**, 1875–1932 (2017).
10. Caulfield, L., Sauter, E., Idriss, H., Wang, Y. & Wöll, C. Bridging the pressure and materials gap in heterogeneous catalysis: A combined UHV, in situ, and operando study using infrared spectroscopy. *J. Phys. Chem. C.* **127**, 14023–14029 (2023).
11. Freund, H. J. et al. Bridging the pressure and materials gaps between catalysis and surface science: clean and modified oxide surfaces. *Top. Catal.* **15**, 201–209 (2001).
12. Assmann, J. et al. Heterogeneous oxidation catalysis on ruthenium: bridging the pressure and materials gaps and beyond. *J. Phys. Condens. Matter* **20**, 184017 (2008).
13. Setvin, M., Wagner, M., Schmid, M., Parkinson, G. S. & Diebold, U. Surface point defects on bulk oxides: atomically-resolved scanning probe microscopy. *Chem. Soc. Rev.* **46**, 1772–1784 (2017).
14. Fu, Q. et al. Interface-confined ferrous centers for catalytic oxidation. *Science* **328**, 1141–1144 (2010).
15. Liang, Z., Li, T., Kim, M., Asthagiri, A. & Weaver, J. F. Low-temperature activation of methane on the IrO_2(110) surface. *Science* **356**, 299–303 (2017).
16. Over, H. Surface chemistry of ruthenium dioxide in heterogeneous catalysis and electrocatalysis: from fundamental to applied research. *Chem. Rev.* **112**, 3356–3426 (2012).
17. Over, H. et al. Atomic-scale structure and catalytic reactivity of the RuO_2(110) surface. *Science* **287**, 1474–1476 (2000).
18. Weaver, J. F., Hakanoglu, C., Antony, A. & Asthagiri, A. High selectivity for primary C-H bond cleavage of propane σ-complexes on the PdO(101) surface. *J. Am. Chem. Soc.* **133**, 16196–16200 (2011).
19. Weaver, J. F., Hakanoglu, C., Antony, A. & Asthagiri, A. Alkane activation on crystalline metal oxide surfaces. *Chem. Soc. Rev.* **43**, 7536–7547 (2014).
20. Huang, W. X. Oxide nanocrystal model catalysts. *Acc. Chem. Res.* **49**, 520–527 (2016).
21. Shi, J. J. et al. High-performance water gas shift induced by asymmetric oxygen vacancies: Gold clusters supported by ceria-praseodymia mixed oxides. *Appl. Catal. B* **301**, 120789 (2022).
22. Jerratsch, J.-F. et al. Electron localization in defective ceria films: A study with scanning-tunneling microscopy and density-functional theory. *Phys. Rev. Lett.* **106**, 246801 (2011).
23. Paier, J., Penschke, C. & Sauer, J. Oxygen defects and surface chemistry of ceria: Quantum chemical studies compared to experiment. *Chem. Rev.* **113**, 3949–3985 (2013).
24. Suntivich, J., May, K. J., Gasteiger, H. A., Goodenough, J. B. & Shao-Horn, Y. A perovskite oxide optimized for oxygen evolution catalysis from molecular orbital principles. *Science* **334**, 1383–1385 (2011).
25. Esch, F. et al. Electron localization determines defect formation on ceria substrates. *Science* **309**, 752–755 (2005).
26. Mullins, D. R. The surface chemistry of cerium oxide. *Surf. Sci. Rep.* **70**, 42–85 (2015).
27. Yang, C. W. et al. Surface faceting and reconstruction of ceria nanoparticles. *Angew. Chem. Int. Ed.* **56**, 375–379 (2017).
28. Muravev, V. et al. Size of cerium dioxide support nanocrystals dictates reactivity of highly dispersed palladium catalysts. *Science* **380**, 1174–1179 (2023).
29. Cargnello, M. et al. Control of metal nanocrystal size reveals metal-support interface role for ceria catalysts. *Science* **341**, 771–773 (2013).
30. Rodriguez, J. A., Grinter, D. C., Liu, Z., Palomino, R. M. & Senanayake, S. D. Ceria-based model catalysts: fundamental studies on the importance of the metal-ceria interface in CO oxidation, the water-gas shift, CO_2 hydrogenation, and methane and alcohol reforming. *Chem. Soc. Rev.* **46**, 1824–1841 (2017).
31. Trovarelli, A. *Catalysis by Ceria and Related Materials*. (Imperial College Press, London, England, 2002).

32. Yang, F. et al. CO Oxidation on inverse CeO_x/Cu(111) catalysts: High catalytic activity and ceria-promoted dissociation of O_2. *J. Am. Chem. Soc.* **133**, 3444–3451 (2011).
33. Yang, C. W. et al. O_2 activation on ceria catalysts-the importance of substrate crystallographic orientation. *Angew. Chem. Int. Ed. Engl.* **56**, 16399–16404 (2017).
34. Kullgren, J. et al. Oxygen vacancies versus fluorine at CeO_2(111): A case of mistaken identity? *Phys. Rev. Lett.* **112**, 156102 (2014).
35. Wu, X.-P. & Gong, X.-Q. Clustering of oxygen vacancies at CeO_2(111): Critical role of hydroxyls. *Phys. Rev. Lett.* **116**, 086102 (2016).
36. Zhu, B. et al. Vacancy ordering in ultrathin copper oxide films on Cu(111). *J. Am. Chem. Soc.* **146**, 15887–15896 (2024).
37. Zhang, Y., Feng, W., Yang, F. & Bao, X. Interface-controlled synthesis of CeO_2(111) and CeO_2(100) and their structural transition on Pt(111). *Chin. J. Catal.* **40**, 204–213 (2019).
38. Fronzi, M., Soon, A., Delley, B., Traversa, E. & Stampfl, C. Stability and morphology of cerium oxide surfaces in an oxidizing environment: A first-principles investigation. *J. Chem. Phys.* **131**, 104701 (2009).
39. Xiao, W. D., Guo, Q. L. & Wang, E. G. Transformation of CeO2(111) to Ce2O3(0001) films. *Chem. Phys. Lett.* **368**, 527–531 (2003).
40. Yang, C. W. et al. Chemical activity of oxygen vacancies on ceria: a combined experimental and theoretical study on CeO_2(111). *Phys. Chem. Chem. Phys.* **16**, 24165–24168 (2014).
41. Nolan, M. & Watson, G. W. The surface dependence of CO adsorption on ceria. *J. Phys. Chem. B* **110**, 16600–16606 (2006).
42. Yang, X. F. et al. Low pressure CO_2 hydrogenation to methanol over gold nanoparticles activated on a CeO_x/TiO_2 interface. *J. Am. Chem. Soc.* **137**, 10104–10107 (2015).
43. Li, H. Y., Wang, H. F., Guo, Y. L., Lu, G. Z. & Hu, P. Exchange between sub-surface and surface oxygen vacancies on CeO_2(111): a new surface diffusion mechanism. *Chem. Commun.* **47**, 6105–6107 (2011).
44. Chu, D. R., Wang, Z. Q. & Gong, X. Q. Theoretical insights into CO oxidation activities on CeO_2(111) steps. *Surf. Sci.* **722**, 122096 (2022).
45. Li, C. et al. Carbon monoxide and carbon dioxide adsorption on cerium oxide studied by Fourier-transform infrared spectroscopy. Part 1.—Formation of carbonate species on dehydroxylated CeO2, at room temperature. *J. Chem. Soc. Faraday Trans.* **85**, 929–943 (1989).
46. Li, N. et al. Size effects of ZnO nanoparticles in bifunctional catalysts for selective syngas conversion. *ACS Catal.* **9**, 960–966 (2019).
47. Sun, J. J. et al. Controllable assembly of CeO_2 micro/nanospheres with adjustable size and their application in Cr(VI) adsorption. *Mater. Res. Bull.* **75**, 110–114 (2016).
48. Perdew, J. P., Burke, K. & Ernzerhof, M. Generalized gradient approximation made simple. *Phys. Rev. Lett.* **77**, 3865–3868 (1996).
49. Perdew, J. P., Burke, K. & Ernzerhof, M. Generalized gradient approximation made simple.*Phys. Rev. Lett.* **78**, 1396–1396 (1997).
50. Kresse, G. & Joubert, D. From ultrasoft pseudopotentials to the projector augmented-wave method. *Phys. Rev. B* **59**, 1758–1775 (1999).
51. Dudarev, S. L., Botton, G. A., Savrasov, S. Y., Humphreys, C. J. & Sutton, A. P. Electron-energy-loss spectra and the structural stability of nickel oxide: An LSDA+U study. *Phys. Rev. B* **57**, 1505–1509 (1998).
52. Da Silva, J. L. F., Ganduglia-Pirovano, M. V., Sauer, J., Bayer, V. & Kresse, G. Hybrid functionals applied to rare-earth oxides: The example of ceria. *Phys. Rev. B.* **75**, 045121 (2007).
53. Huang, M. & Fabris, S. CO adsorption and oxidation on ceria surfaces from DFT+U calculations. *J. Phys. Chem. C* **112**, 8643–8648 (2008).
54. Loschen, C., Carrasco, J., Neyman, K. M. & Illas, F. First-principles LDA+U and GGA+U study of cerium oxides: Dependence on the effective U parameter. *Phys. Rev. B* **84**, 199906 (2007).

Acknowledgements

This work was financially supported by the National Natural Science Foundation of China (21991152 (Z.L.), M-0384 (F.Y.)), National Key R&D Program of China (2022YFA1503802, F.Y.) and Shanghai-XFEL Beamline Project (SBP) (3101150550588592016 1A2101001, Z.L.). The authors thank the support from the Analytical Instrumentation Center, at ShanghaiTech University and BL02B01 of the Shanghai Synchrotron Radiation Facility (SSRF) supported by the National Natural Science Foundation of China (11227902, Z.L.). DFT calculations were performed at Brookhaven National Laboratory, which was supported by the U.S. Department of Energy (DOE), Office of Science, Office of Basic Energy Sciences, Division of Chemical Sciences, Biosciences and Geosciences, under contract No. DE-SC0012704 (P.L.).

Author contributions

W.S., Y.Z., and Z.W.Z. contributed equally to this work. Y. Z. carried out STM/XPS experiments. Z.W.Z. and P.L. carried out DFT calculations. W.S. carried out model catalytic tests and quasi-in-situ XPS experiments. W.S., N.L., and F.J. carried out the powder catalytic measurements. W.S. carried out FT-IR experiments. Y.S.L., Y.C., and Y.J.L. participated in SRPES experiments. Z.Y.Z. carried out NAPXPS experiments. Z.L., X.P., Q.F., and C.W. participated in the discussion and analysis of experimental results. W.S., Y.Z., Z.W.Z., P.L., and F.Y. analyzed the data and wrote the draft. F.Y. constructed and wrote the paper. X.B. and F.Y. designed and supervised the project.

Competing interests

The authors declare no competing interests.

Additional information

Supplementary information The online version contains supplementary material available at https://doi.org/10.1038/s41467-024-53948-1.

Correspondence and requests for materials should be addressed to Fan Yang.

Peer review information *Nature Communications* thanks Gyeong-Su Park and the other anonymous reviewers for their contribution to the peer review of this work. A peer review file is available.